Probing Vacuum Energy via a Bell–Casimir–Squeezing–Spectroscopy Quartet

Zachary, D.S.

Energy Policy and Climate Program Johns Hopkins, Krieger School of Arts and Sciences, 555 Pennsylvania Avenue, NW Washington, D.C. 20001

E-mail: d.s.zachary@jhu.edu

Abstract. The ER=EPR conjecture posits a fundamental link between quantum entanglement and spacetime geometry, suggesting that entangled particles may be connected via an entanglement–geometry correspondence. Direct experimental tests are challenging due to the Planck-scale nature of such effects; however, recent theoretical models predict that entanglement could induce small but measurable modifications to vacuum energy and stress–energy correlations. Here, we present an integrated experimental platform combining high-fidelity Bell inequality tests, precision Casimir force measurements, and quantum optical squeezing in interferometric setups to probe these signatures. Each modality targets vacuum fluctuations and quantum correlations, enabling a correlation-based approach to explore the entanglement–geometry correspondence. We describe the theoretical framework, experimental design, and signal extraction techniques, including principal component analysis and mutual information, for detecting subtle anomalies. Our results establish new bounds on entanglement-induced modifications to quantum vacuum behavior and propose a scalable pathway for investigating foundational aspects of spacetime using tabletop quantum optics.

Keywords: ER=EPR conjecture, quantum entanglement, Casimir effect, Bell inequality, vacuum energy, entanglement–geometry correspondence

Submitted to: *Quantum Science and Technology*

1. Introduction

The relationship between quantum entanglement and spacetime geometry has gained renewed attention with the conjecture that Einstein–Rosen bridges (wormholes) and Einstein–Podolsky–Rosen (EPR) entanglement may be physically equivalent—known as the ER=EPR conjecture [2, 4]. Building on earlier insights linking entanglement to geometric connectivity in holography [5], this idea has inspired theoretical proposals suggesting that spacetime itself may emerge from quantum information. However, experimental probes of this conjecture remain scarce due to the presumed Planck-scale nature of such effects.

Recent models suggest that entanglement-induced modifications to vacuum energy or stress–energy correlations could produce subtle, low-energy signatures [6, 31]. Motivated by this possibility, we explore precision experiments capable of detecting these signatures through established quantum measurement techniques. Our approach integrates four complementary modules—entangled photon sources (S), optical squeezing stages (SQ), optomechanical Casimir cavities (CM/OM), and high-finesse spectroscopy loops (H)—to probe vacuum fluctuations, quantum correlations, and potential entanglement-induced deviations from standard quantum field theory (QFT).

These observables access distinct but complementary aspects of quantum field theory in curved or bounded spacetimes. Entangled photons generated via spontaneous parametric down-conversion [10] enable Bell tests with spacelike-separated analyzers, probing nonlocal correlations. The Casimir cavity, enhanced with an embedded compliant optomechanical membrane, is exquisitely sensitive to boundary conditions, geometry, and stress-energy perturbations [15, 16, 22], potentially revealing deviations if vacuum energy responds to quantum correlations. Optical squeezing, routinely used in gravitational wave detectors, provides quantum-enhanced phase sensitivity and access to sub-vacuum fluctuations [18, 19]. High-finesse spectroscopy further enables precision probing of frequency shifts or energy-level modifications induced by entanglement–vacuum–optomechanical interactions.

Rather than attempting to detect entanglement–geometry correspondence (Planck-scale wormholes) directly, our goal is to place new experimental constraints on entanglement-induced deviations from standard QFT. We emphasize data-driven approaches, including signal modeling, statistical sensitivity analysis, and correlation extraction using tools such as principal component analysis (PCA) [27] and mutual information [28]. These methods allow anomaly detection even when signatures are subtle, mediated through the optomechanical module, or distributed across multiple experimental channels.

This paper is organized as follows. Section 2 reviews the experimental implementation of the Bell–Casimir–Squeezing–Spectroscopy–Optomechanical quartet. Section 3 presents the theoretical framework linking entanglement to vacuum modifications. Section 4 details signal extraction and correlation analysis methods. Section 5 presents falsification sensitivity analysis. Section 6 explores alternative

experimental pathways, followed by next-generation proposals in Section 7. Section 8 summarizes conclusions and discusses future directions.

2. Experimental Platforms: Bell–Casimir–Squeezing–Spectroscopy Quartet

2.1. Bell Test Platform

The experimental configuration begins with the generation of polarization-entangled photon pairs via spontaneous parametric down-conversion (SPDC) [10]. One photon is directed to Alice, and its entangled partner is sent to Bob. Alice's photon passes through a polarization selector and is detected by detector D_A. Bob's photon traverses a vacuum cavity containing an embedded optomechanical membrane, and may also pass through an optical squeezing stage, before reaching his polarization analyzer and detector D_B. Coincidence counts between D_A and D_B are used to compute the Clauser–Horne–Shimony–Holt (CHSH) correlation. The goal is to detect perturbations in the Bell signal at the $\sim 10^{-6}$ level [8, 9].

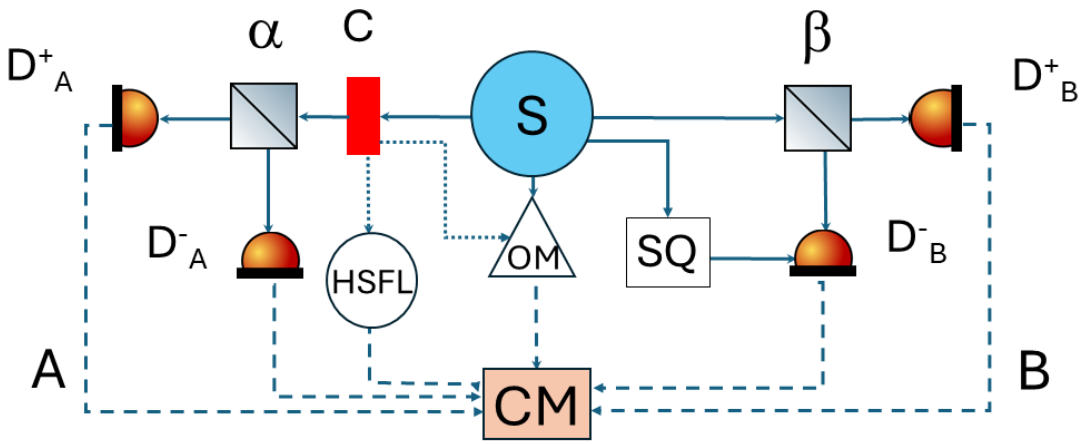

Figure 1: Schematic of the hybrid experimental setup integrating four modules: (1) a Bell-type entangled photon source (S) producing spatially separated photon pairs along arms A and B; (2) an optical squeezing stage (SQ) inserted in Bob's arm; (3) an optomechanical Casimir cavity (CM) also in Bob's arm; and (4) a high-finesse spectroscopy loop (H). Beam splitters (α, β) and detectors ($D_A^{\pm}$, $D_B^{\pm}$) implement Bell measurements. Coincidence monitoring defines the observables used to establish the sensitivity thresholds shown in the falsification diagrams of Section 5. Arrows indicate the primary (solid) and mediated or vacuum-modified (dotted) pathways that carry quantum correlations between modules for ER=EPR tests.

The CHSH Bell observable is defined as

$$S = |E(a,b) + E(a,b') + E(a',b) - E(a',b')| \leq 2, \tag{1}$$

where $E(a,b)$ is the polarization correlation function for measurement settings a and b. Under standard quantum theory, S depends only on the entangled state and measurement bases. However, if vacuum fluctuations or optomechanical modifications influence the entanglement or measurement statistics, a geometry-dependent shift in S may arise. We parametrize this effect as

$$S(d) = S_0 + \delta S(d), \tag{2}$$

where S_0 is the baseline Bell value in an unmodified vacuum (typically $S_0 \approx 2.5$), and $\delta S(d)$ is a displacement-dependent perturbation related to cavity separation d, optomechanical coupling, or vacuum modifications induced by the membrane [29, 31]. This perturbation defines the Bell-threshold curves used in the falsification diagrams of Section 5. Details of the mapping into threshold curves are provided in Appendix Appendix D.

2.2. Casimir–Optomechanical Module

A compliant membrane placed inside a Casimir cavity along Bob's photon path modifies boundary conditions for vacuum modes. If entanglement affects the local stress-energy tensor, this can manifest as measurable shifts in the membrane's equilibrium position, resonance frequency, or induced optomechanical displacement [16, 22]. For any vacuum-sensitive observable X, the entanglement-induced deviation is defined as

$$\Delta X = X_{\text{ent}} - X_0, \tag{3}$$

where X_{ent} is measured under entangled conditions and X_0 is the baseline value without entanglement effects.

The minimum detectable displacement is limited by the standard quantum limit (SQL),

$$\delta x_{\text{SQL}} \approx \sqrt{\frac{\hbar}{2m\omega_m}}, \tag{4}$$

where m is the membrane mass and ω_m its mechanical resonance frequency. This SQL sets the Casimir detection boundary, which appears as a sensitivity threshold in the falsification diagrams (Appendix C). OM displacements also provide indirect contributions to Bell and spectroscopy observables through vacuum-modulated correlations.

2.3. Optical Squeezing Channel

An optical parametric oscillator (OPO) generates squeezed vacuum states, reducing noise in one quadrature while amplifying it in the conjugate quadrature [17]. If vacuum fluctuations are modified by the Casimir cavity, optomechanical module, or membrane, the squeezing parameter r may exhibit geometry-dependent perturbations [29, 30].

The squeezed quadrature variance is

$$\Delta^2 X_{\text{squeezed}} = \frac{\hbar}{2} e^{-2r}, \tag{5}$$

with r quantifying squeezing strength. Small changes in $r(d)$ induce corresponding shifts in the Bell observable,

$$\delta S(d) \sim \alpha \frac{\partial r}{\partial d}, \tag{6}$$

where α encodes the experimental sensitivity of Bell measurements to squeezing variations. These shifts define the squeezed-Bell threshold used in the falsification framework (Appendix C).

2.4. Spectroscopy Loop Readout

Downstream of the vacuum cavity, a high-finesse Fabry–Pérot spectroscopy loop with Pound–Drever–Hall (PDH) locking detects phase variations [18]. Vacuum polarization changes, Casimir effects, and optomechanical displacements modify the effective refractive index, producing a phase shift

$$\delta\phi_{\text{loop}} = \frac{4\pi L}{\lambda} \frac{\delta n}{n}, \tag{7}$$

where L is the optical path length, λ the probe wavelength, and δn the index perturbation. This readout provides a sensitive cross-check observable in the falsification diagrams (Appendix C).

2.5. Signal Detection and Noise Considerations

All observables are measured statistically, so the Bell signal can be modeled as

$$S = S_0 + \Delta S + \xi(t), \tag{8}$$

where ΔS is the deterministic shift from geometry, optomechanical effects, or entanglement, and $\xi(t)$ is background noise. The relation between ΔS, membrane displacement Δx, squeezing variance $\Delta^2 X_{\text{squeezed}}$, spectroscopy loop phase $\delta\phi_{\text{loop}}$, and optomechanical signals is derived in Appendix C.

The signal-to-noise ratio (SNR) is

$$\text{SNR} = \frac{\langle \Delta S \rangle}{\sigma_S}, \tag{9}$$

with $\langle \Delta S \rangle$ the mean signal shift and σ_S the noise standard deviation over repeated trials. These thresholds feed directly into the falsification sensitivity analysis of Section 5.

The integration of the *four modules—Bell violation tracking, Casimir–optomechanical modulation, optical squeezing, and high-finesse spectroscopy loop readout*—constitutes a comprehensive platform for detecting vacuum-mediated entanglement effects. Multi-channel correlation of small shifts in S, Δx, $\Delta^2 X_{\text{squeezed}}$, $\delta\phi_{\text{loop}}$, and OM signals offers a promising pathway to experimentally probe the ER=EPR hypothesis in controlled laboratory settings. These observables also define the sensitivity curves used to generate the falsification diagrams (Section 5).

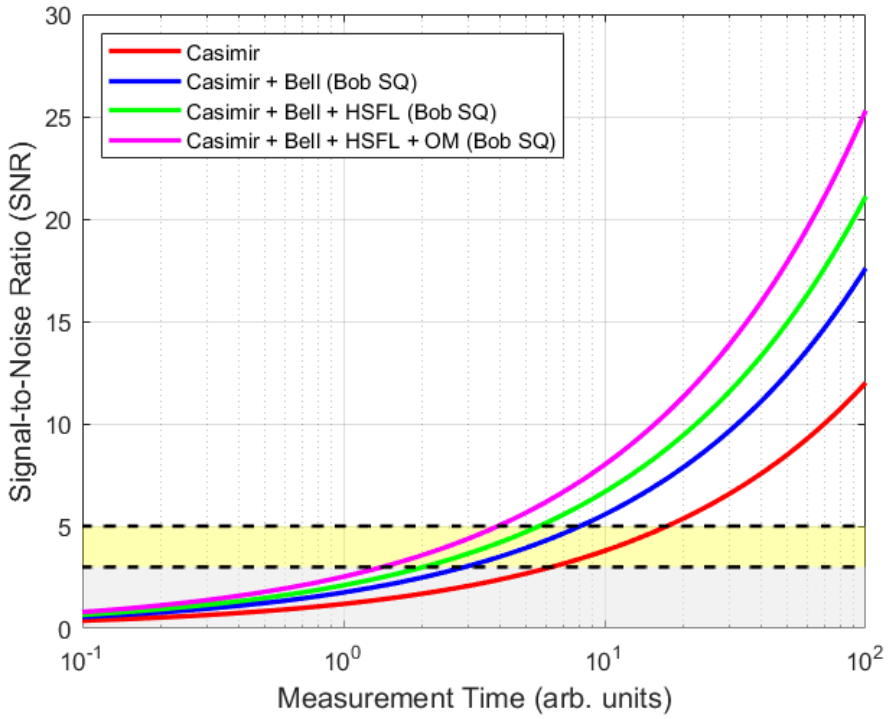

Figure 2: Simulated signal-to-noise ratio (SNR) scaling for the hybrid experimental setup. Red, blue, green, and magenta curves correspond to Casimir-only, Casimir plus Bell (with Bob's squeezing), Casimir plus Bell plus HSFL contributions, and Casimir plus Bell plus HSFL plus optomechanical (OM) contributions, respectively. Shaded regions indicate statistical detection thresholds: gray for weak falsification and yellow for strong falsification. Dashed lines denote threshold boundaries. Mapping from theoretical perturbations (ΔS, Δx, $\Delta^2 X_{\text{squeezed}}$, $\delta\phi_{\text{loop}}$, OM displacement signals) to these SNR curves is provided in Appendix C.

Category	**Mechanism / Theoretical Model**	**Affected**
Enhancement Mechanisms		
Entanglement-induced $\langle T_{\mu\nu}\rangle$ shifts	Entanglement alters stress-energy tensor, producing measurable pressure or refractive changes [31]	B, C, O
Vacuum polarization coupling	Nonlocal wormhole links perturb vacuum or field modes [29]	S, H
Backreaction from ER foam	Fluctuating ER bridges influence effective geometry [6]	B, C, H
Boundary modif. via ER=EPR	Cavity entanglement modifies boundary field constraints [4]	B, C, H
Loop-amplified coherence	Long paths in HFSL readout enhance phase sensitivity [19]	H
Suppression Mechanisms		
Environmental decoherence	Thermal/EM noise reduces entanglement fidelity [12]	B, S, O
Photon loss in cavities	Finite Q degrades squeezing and phase locking [17]	S, H
Mechanical damping	Low Q resonators filter out weak vacuum force signals [21]	O
Shot noise & dark counts	Background noise limits Bell and squeezing SNR [8]	B, S
Mode mismatch (HFSL)	Imperfect PDH locking smears sub-femtometer phase [19]	H

Table 1: Theoretical mechanisms that either enhance or suppress quantum vacuum observables under the ER=EPR framework. B = Bell, C = Casimir, S = Squeezing, O = Optomechanical, H = HFSL loop. These mechanisms motivate the sensitivity thresholds and anomaly regions introduced in Section 5. The quantitative mapping from theoretical perturbations to observable shifts (ΔS, Δx, $\Delta^2 X_{\text{squeezed}}$, $\delta\phi_{\text{loop}}$) is provided in Appendix C.

3. Theoretical Framework and Motivations

3.1. Entanglement and Spacetime Geometry

The ER=EPR conjecture posits a fundamental equivalence between quantum entanglement and nontraversable Einstein–Rosen (ER) bridges [2,4]. In this framework, entangled pairs correspond to microscopic wormholes linking spacetime regions without permitting classical information transfer. This duality suggests that the structure of spacetime geometry may emerge from the pattern of quantum entanglement [5], implying that entanglement could have subtle geometric and physical consequences at low energies.

3.2. Vacuum Energy and Casimir Geometry

Vacuum fluctuations respond sensitively to boundary conditions, as exemplified by the Casimir effect, where the exclusion of vacuum modes between conducting plates generates an attractive force [14, 15]. Since entanglement alters the quantum state of fields, it is natural to ask whether the local vacuum expectation value of the stress-energy tensor, $\langle T_{\mu\nu}\rangle$, can be perturbed in an entanglement-dependent manner [29–31]. Such perturbations could modify vacuum pressure, electromagnetic mode structure, or refractive indices inside cavities, motivating precision measurements under controlled entangled states.

3.3. Stress-Energy Shift Hypothesis

We hypothesize that entangled quantum fields produce a shift in vacuum stress-energy relative to the unentangled vacuum,

$$\delta\langle T_{\mu\nu}\rangle = \langle T_{\mu\nu}\rangle_{\text{ent}} - \langle T_{\mu\nu}\rangle_0, \tag{10}$$

where $\langle T_{\mu\nu}\rangle_{\text{ent}}$ denotes the expectation value in the presence of entanglement and $\langle T_{\mu\nu}\rangle_0$ the standard vacuum. This shift may depend on the entanglement entropy, purity, or spatial separation of subsystems [30, 31]. Detecting such a shift would manifest as measurable deviations in Casimir forces, optical phase shifts, squeezing parameters, or membrane displacements. These shifts form the theoretical underpinning of the sensitivity thresholds introduced later in Section 5.

3.4. Operational Probes and Experimental Signatures

Directly probing Planck-scale geometry remains impractical; therefore, we focus on experimentally accessible observables sensitive to vacuum modifications induced by entanglement. These include Bell inequality violations with spacelike-separated detectors, Casimir-induced mechanical displacements, squeezing parameters in quantum optics, phase shifts in high-finesse spectroscopy loops, and optomechanical (OM) displacements of compliant membranes [21, 29, 30]. Changes in these observables

correlated with entanglement structure could serve as indirect witnesses of an underlying spacetime–entanglement correspondence.

The expected enhancement and suppression mechanisms for these observables, across Bell (B), Casimir (C), Squeezing (S), HFSL (H), and optomechanical (OM) modules, are summarized in Table 1. Their associated thresholds define the boundary curves appearing in the falsification diagrams of Section 5. These scaling behaviors are illustrated in Figure 2, which shows the simulated signal-to-noise ratio response of the integrated setup under shot-noise-limited detection.

3.5. Model-Agnostic Experimental Strategy

Our approach remains agnostic to specific quantum gravity theories, emphasizing empirical detection of correlations between entanglement and vacuum response. This parallels decoherence and quantum noise studies in matter interferometry, which constrain fundamental physics through precision measurement without assuming particular models [9]. By combining Bell tests, Casimir geometry, squeezing-based readouts, high-finesse spectroscopy loops, and optomechanical monitoring of compliant membranes, we construct a hybrid platform capable of revealing subtle entanglement-induced modifications to vacuum observables. This motivates the falsification-based strategy developed later, where overlapping anomalies in Bell, Casimir, squeezing, spectroscopy, and optomechanical observables define testable regions for ER=EPR.

4. Data Analysis and Signal Extraction

The hybrid experiment integrates multiple quantum-optical components, each contributing distinct observables: Bell correlations, cavity-induced phase shifts, optical squeezing variances, Casimir-induced membrane displacements, and optomechanical (OM) signals. All data streams are synchronized via shared timestamps and processed jointly to extract entanglement-induced deviations relative to calibrated vacuum baselines [9, 31].

4.1. Coincidence-Based CHSH Measurement

Photon detection events at D_A and D_B are time-tagged, and correlation terms $E(a, b)$ are extracted from joint detection probabilities. The standard CHSH quantity is then

$$S = |E(a, b) + E(a, b') + E(a', b) - E(a', b')|. \tag{11}$$

Small shifts,

$$\Delta S = S_{\text{ent}} - S_0, \tag{12}$$

are identified by comparing entangled photon runs with non-entangled baselines [8].

4.2. Membrane and Optomechanical Displacement Readout

The compliant membrane inside the Casimir cavity, coupled to the optomechanical module, responds to vacuum-pressure fluctuations. Interferometric or cavity-enhanced readout provides the displacement $x(t)$, from which we extract

$$\Delta x = x_{\text{ent}} - x_0. \tag{13}$$

Thermal, seismic, and optomechanical back-action contributions are filtered in post-processing. The fundamental limit is set by the standard quantum limit (SQL),

$$\delta x_{\text{SQL}} = \sqrt{\frac{\hbar}{2m\omega_m}}, \tag{14}$$

where m is the effective motional mass and ω_m the mechanical resonance frequency.

4.3. Squeezing Variance Tracking

The OPO stage in Alice's arm generates squeezed states with reduced quadrature variance. The relevant deviation is

$$\Delta^2_{\text{squeezed}} = \langle \Delta X^2 \rangle - \langle \Delta X^2 \rangle_0, \tag{15}$$

with X the quadrature operator of interest.

4.4. Phase Loop Monitoring

The high-finesse spectroscopy loop, stabilized using the Pound–Drever–Hall (PDH) method, measures small downstream phase shifts. The monitored observable is

$$\delta\phi_{\text{loop}} = \phi_{\text{ent}} - \phi_0. \tag{16}$$

4.5. Combined Sensitivity Estimate

For each observable $\mathcal{O}$, the minimum resolvable deviation is modeled as

$$\delta\mathcal{O}_{\min} = \frac{\sigma_{\mathcal{O}}}{\sqrt{N}} + \delta_{\text{sys}}(\mathcal{O}), \tag{17}$$

where $\sigma_{\mathcal{O}}$ is the statistical spread over N events, and δ_{sys} denotes systematic uncertainty [26]. These limits establish the sensitivity baselines for the falsification diagrams.

4.6. Cross-Correlated Multi-Channel Pipeline

All observables—Bell correlations, membrane/optomechanical displacements, squeezing variances, and phase shifts—are time-synchronized and analyzed in parallel. Events displaying correlated anomalies across two or more channels are prioritized as potential ER=EPR signatures. This multi-channel pipeline underlies the falsification strategy of Section 5, where overlapping deviations in independent observables define robust regions of sensitivity and exclusion.

5. Falsification Sensitivity Analysis

The hybrid Bell–Casimir–squeezing–spectroscopy platform enables falsifiable bounds on the ER=EPR conjecture. We introduce falsification sensitivity diagrams that map minimum detectable shifts in each observable onto parameter-space domains where ER=EPR-related effects would be confirmed, falsified, or remain ambiguous. These diagrams combine thresholds derived in Sections 2–4 with multi-channel cross-correlation strategies.

5.1. Casimir, Bell, Squeezing, and Optomechanical Thresholds

The first falsification diagram compares sensitivity thresholds for Casimir displacement measurements, Bell correlations, squeezing enhancements, and optomechanical modulation. The Casimir limit is set by the SQL displacement of Eq. (14), while the Bell threshold arises from the minimal detectable perturbation in the CHSH parameter of Eq. (12). Squeezing-enhanced Bell thresholds incorporate geometry-dependent perturbations to the quadrature variance of Eq. (15), and the optomechanical module (OM) provides additional vacuum-sensitive displacement readout [16, 22].

Figure 3 illustrates these thresholds in the $(t, \Delta\mathcal{O})$ plane, where t denotes integration time and $\Delta\mathcal{O}$ a generic observable shift. Four domains appear naturally: (i) a gray region below all thresholds where no detection is possible; (ii) an intermediate yellow region above a single threshold where anomalies cannot be uniquely classified; (iii) a red overlap region above Casimir and Bell–squeezing thresholds; and (iv) a dark green overlap region where Casimir, Bell, squeezing, and optomechanical thresholds are simultaneously exceeded, indicating the strongest potential ER=EPR signature.

5.2. Overlay with Alternative Experiments

To test robustness, thresholds from additional experimental pathways are superimposed, including atom interferometry, gravitational-wave strain detectors, and superconducting qubits. Each defines a detection boundary, and their overlaps delineate regions where cross-confirmation is possible. Light shading indicates twofold confirmation; darker shading indicates three or more simultaneous detections. Multi-experiment overlay strengthens falsification by demanding consistency across independent physical platforms.

5.3. Classification of Anomalies

Outcomes are interpreted according to diagram regions. If anomalies appear in the dark green overlap region (Casimir + Bell + Squeezing + OM), this constitutes strong evidence for entanglement-induced vacuum modifications. If only one or two thresholds are crossed, the signal is ambiguous and may reflect systematic errors. If no anomalies exceed thresholds, ER=EPR-related effects are falsified at the tested scale. The

strongest evidence arises when anomalies lie in multi-experiment overlap zones, ruling out single-platform artifacts.

5.4. Integration with Statistical Tools

Shaded regions in Fig. 3 correspond to anomaly significance classes. Appendix Appendix A supplements this with principal component analysis (PCA), mutual information, and cross-correlation to identify correlated deviations. Additional statistical tests, including chi-squared consistency and Kullback–Leibler divergence, quantify departure from null distributions. Bootstrapped thresholding further constrains false-positive rates. Overall sensitivity trends are summarized in Fig. 2, which now plots *linear–log* (lin–log) scaling of sensitivity versus measurement time to emphasize early-time linear behavior and long-time exponential decay.

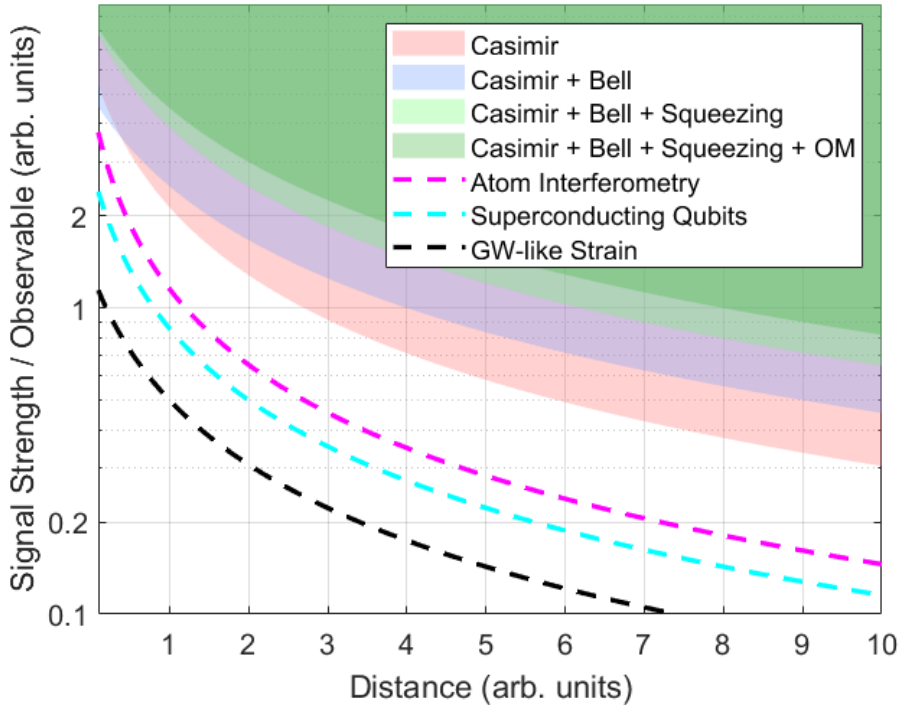

Figure 3: Unified sensitivity diagram across experimental platforms, including the optomechanical (OM) module. Shaded regions correspond to detection domains for Casimir (red), Bell correlations (blue), Bell–squeezing enhancements (green), and Casimir + Bell + Squeezing + Optomechanical (dark green). Dashed lines represent candidate extensions: atom interferometry (magenta), superconducting qubits (cyan), and gravitational-wave strain measurements (black). Compact observables are defined in Eqs. 12–16. This figure highlights multi-channel thresholds and overlap zones that provide robust falsification regions for the ER=EPR hypothesis.

5.5. Compact Observable Models

To compare disparate experiments, we define normalized observables $\mathcal{O}(d)$ or $\mathcal{O}(t)$ capturing geometry and quantum resources.

Casimir observable. The Casimir pressure is

$$P(d) = -\frac{\pi^2 \hbar c}{240\, d^4}, \tag{18}$$

with normalized form

$$\mathcal{O}_{\mathrm{C}}(d) = \frac{P(d)}{P(d_{\mathrm{ref}})} = \frac{(d_{\mathrm{ref}})^4}{(d + d_0)^4}, \tag{19}$$

where d_0 regularizes non-idealities.

Entanglement-weighted Casimir observable ("Bell"). Entanglement visibility $V(d)$ is modeled as e^{-d/L_0}:

$$\mathcal{O}_{\mathrm{C+B}}(d) = \mathcal{O}_{\mathrm{C}}(d)\, e^{-d/L_0}. \tag{20}$$

Squeezing-enhanced observable. With squeezing parameter $r(d) = r_0 e^{-d/L_s}$, the multiplier $e^{r(d)}$ enhances sensitivity:

$$\mathcal{O}_{\mathrm{C+B+S}}(d) = \mathcal{O}_{\mathrm{C}}(d)\, e^{-d/L_0}\, e^{\,r_0 e^{-d/L_s}}. \tag{21}$$

Optomechanical-enhanced observable. Optomechanical displacement Δx_{OM} contributes an additional factor:

$$\mathcal{O}_{\mathrm{C+B+S+OM}}(d) = \mathcal{O}_{\mathrm{C+B+S}}(d)\, (1 + \Delta x_{\mathrm{OM}}(d)/x_{\mathrm{ref}}). \tag{22}$$

Other candidate platforms. Atom interferometers yield $\mathcal{O}_{\mathrm{AI}}(T) = (T/T_{\mathrm{ref}})^2$, superconducting qubits yield $\mathcal{O}_{\mathrm{Q}}(t) = \exp[-(t - t_{\mathrm{ref}})/T_2]$, and gravitational-wave strain detectors yield $\mathcal{O}_{\mathrm{GW}}(f) = h(f)/h(f_{\mathrm{ref}})$.

5.6. Time–Distance Mapping

Signals propagating at group velocity v_g obey

$$d = v_g\, t \quad \Longrightarrow \quad \mathcal{O}(t) = \mathcal{O}(d = v_g t). \tag{23}$$

When Casimir scaling dominates we plot versus d; when coherence time dominates (e.g. Bell runs) we plot versus t. On log–log axes, power laws (e.g. d^{-4}) appear as straight lines, while exponentials (e^{-d/L_0}) appear as curvature, making falsification diagrams visually diagnostic.

6. Alternative Experimental Pathways

In addition to the core Bell–Casimir–squeezing setup, several alternative platforms provide independent avenues for probing entanglement-induced modifications to vacuum observables. These approaches differ in sensitivity, scale, and cost, but collectively serve as valuable cross-checks or indirect probes of ER=EPR-like effects [4, 31].

Atomic clocks and time-of-flight interferometry. Optical lattice clocks and matter-wave interferometers can detect fractional frequency shifts as small as $\Delta\nu/\nu \sim 10^{-19}$ [43]. While direct evidence of entanglement-modified vacuum energy is lacking, gravitational decoherence models suggest that phase instabilities may arise in entangled matter-wave interferometers such as MAGIS-100 [44]. A representative time-of-flight phase sensitivity can be modeled as

$$\delta\phi_{\mathrm{ToF}} \sim k_{\mathrm{eff}}\, a\, T^2, \tag{24}$$

where k_{eff} is the effective wavevector, a the acceleration, and T the interrogation time.

Atomic interferometry. Long-baseline atomic interferometers measure phase shifts in matter waves due to inertial or gravitational effects [45]. If entanglement alters the local vacuum stress–energy tensor, differential phase shifts as small as $\phi \sim 10^{-6}$ radians may emerge. Projects like AION [46] and MAGIS are approaching the sensitivity required to detect such effects over kilometer-scale baselines.

Rotational experiments. Sagnac-type gyroscopes and fiber-optic rotation sensors achieve angular resolution down to $\theta \sim 10^{-11}$ radians [42]. Some ER=EPR-inspired models suggest that entanglement across rotating frames could subtly modify inertial frame detection. While speculative, these devices provide low-cost, high-stability platforms for testing correlations tied to entanglement.

Accelerators and colliders. High-energy particle collisions, such as those at the LHC or proposed next-generation colliders, may indirectly reveal deviations in entropy or energy distributions if Planck-scale entanglement modifies final-state vacuum configurations [7]. Expected shifts in final-state entropy,

$$\Delta S_{\mathrm{ent}} \sim 10^{-3}, \tag{25}$$

remain extremely challenging to disentangle from thermalization and QCD backgrounds. Current collider precision is still orders of magnitude away from probing ER=EPR-relevant regimes.

Holographic noise measurements. Experiments such as the Fermilab Holometer attempt to detect Planck-scale transverse position noise,

$$\langle \delta x_\perp^2 \rangle \sim 10^{-20}\ \mathrm{m}^2, \tag{26}$$

predicted by holographic uncertainty principles [40, 41]. If ER=EPR links span interferometer arms, these nonlocal correlations could enhance the measured noise floor. While previous results are consistent with null, this approach remains a promising low-cost tabletop test of vacuum geometry.

Optomechanical cavities. High-Q optomechanical systems provide complementary sensitivity to sub-vacuum fluctuations [16, 22]. Membrane-in-the-middle setups, microtoroids, or suspended mirrors can probe Casimir-modulated or entanglement-enhanced displacements. By integrating OM modules with squeezed-light or Bell tests, correlations between mechanical motion and optical observables can strengthen falsification strategies, extending the reach of the core platform.

These alternative approaches collectively extend the experimental landscape for testing whether entanglement can modify vacuum observables in ways consistent with ER=EPR. While some remain speculative or limited by systematics, cross-confirmation with the core Bell–Casimir–squeezing-optomechanical platform enhances robustness and provides access to complementary parameter regimes.

7. Next Generation Experiments

Beyond current tabletop capabilities, several large-scale or emerging quantum platforms have been proposed to test correlations between entanglement and vacuum structure. While many of these remain technically or interpretively challenging, they offer future potential for constraining ER=EPR-motivated modifications to quantum field observables [4,31]. Figure 4 compares estimated cost against required sensitivity across sixteen experimental platforms, highlighting tradeoffs between feasibility and scalability.

Cosmic Microwave Background (CMB): The observable is the angular power spectrum C_ℓ. Anomalies at large scales could encode early-universe quantum correlations. Under some ER=EPR interpretations, entanglement across causally disconnected regions may induce coherent phase modulations [1]. Future missions such as LiteBIRD and CMB-S4 aim for sensitivity

$$\frac{\Delta C_\ell}{C_\ell} \sim 10^{-6}, \tag{27}$$

potentially constraining such effects [35, 36].

Gravitational Lensing: The relevant observables are weak-lensing convergence κ, shear γ, and deflection α. These may be subtly affected by entanglement-modified stress-energy across large-scale structures. While model-dependent, surveys like Euclid, Roman, and LSST may constrain long-range nonlocal vacuum effects through deviations in lensing PDFs at the level of

$$\delta\kappa \sim 10^{-4}, \tag{28}$$

as discussed in [37–39].

Cosmic Voids: The observable is the two-point void correlation ξ_{void}. Entanglement-induced topology could alter void clustering statistics, with predicted shifts

$$\delta\xi_{\text{void}} \sim 10^{-3}. \tag{29}$$

While not yet observable, next-generation void catalogs may place indirect bounds on such models [3, 31].

Superconducting Qubits and Quantum Dots: The observable is coherence time T_2. If stress-energy fluctuations are modulated by entanglement structure, coherence times may shift as

$$\delta T_2 \sim \frac{G\,\delta\rho\,L^2}{\hbar}, \tag{30}$$

where L is the qubit cavity length [21]. Quantum dots may similarly exhibit minute tunneling or energy-level shifts, though isolating such effects remains speculative and model-dependent [32].

Gravitational Wave Detectors: The observable is spacetime strain $h(t)$. Instruments such as LIGO, Virgo, and future observatories (e.g., LISA, Einstein Telescope) probe strain with sensitivity $h \sim 10^{-23}/\sqrt{\text{Hz}}$ [47]. The canonical measurement is

$$h(t) = \frac{\Delta L(t)}{L}, \tag{31}$$

which could incorporate nonclassical structure if spacetime geometry is entanglement-governed. Current data impose no such signal, but long-term stochastic analyses may tighten constraints [47–49].

Pulsar Timing Arrays (PTAs): The observable is the timing residual $\delta t(t)$. PTAs monitor millisecond pulsars to detect long-wavelength metric perturbations. An effective entanglement-modified strain h_{eff} would produce a shift

$$\delta t(t) \sim \frac{L}{2c}\,h_{\text{eff}}. \tag{32}$$

While primarily developed for gravitational wave detection, isotropic and temporally incoherent timing noise could serve as an indirect test of ER=EPR-style geometry [33, 34].

These next-generation platforms collectively explore parameter regimes inaccessible to current tabletop experiments. While ER=EPR-specific signatures remain hypothetical, the combination of high sensitivity, large scale, and cross-correlated observables could ultimately provide stringent indirect constraints on entanglement-modified spacetime structure.

8. Summary and Conclusions

In this work, we have proposed a set of experimental frameworks to test whether quantum entanglement can modify local vacuum energy observables, in line with the ER=EPR conjecture [4, 31]. The central hypothesis is that entangled systems

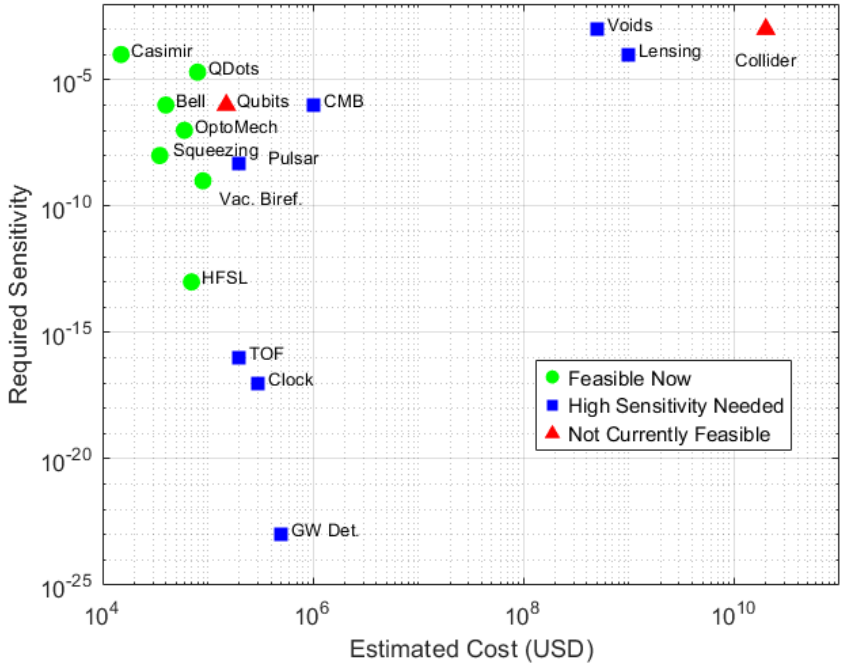

Figure 4: Log–log plot comparing estimated cost and required sensitivity for 16 experimental platforms. Markers indicate feasibility categories: green circles (feasible now), blue squares (higher sensitivity required), red triangles (not currently feasible). This figure highlights tradeoffs between achievable precision, platform scale, and resource investment.

may imprint correlations on vacuum-sensitive measurements—such as Casimir forces, squeezing variances, and optical path shifts—thereby allowing indirect detection of underlying entanglement structures, including potential wormhole-like connections.

We surveyed eighteen experimental approaches, evaluating each in terms of sensitivity, cost, scalability, and relevance to ER=EPR. Particular emphasis was placed on hybrid optical systems that integrate entangled photon sources with compliant mechanical or optomechanical components, where classical stress-energy observables can be directly modulated by quantum correlations. Alternative and next-generation methods—including atomic clocks, gravitational lensing, pulsar timing arrays, and holographic noise detection—were also reviewed to provide a comprehensive perspective.

To assess the feasibility of detecting ER=EPR-type effects with realistic detectors, Appendix A presents a series of simulated measurements for three representative observables: Bell violation (S), Casimir force shift (ΔF), and squeezing variance (ΔV_{sq}). A small fraction of events (10%) were seeded with entanglement-enhanced correlations across all channels. Analytical projections show that even this modest signal fraction produces detectable structure in the principal component space (Fig. App 1), cross-correlation patterns (Fig. App 2), mutual information matrices (Fig. App 3), and histograms of multi-channel deviations (Fig. App 4), clearly distinguishing quantum-enhanced signals from classical baselines.

While still exploratory, these methods illustrate a model-agnostic, tabletop strategy

for probing Planck-scale structure with current or near-future quantum instrumentation. In particular, multi-channel anomaly detection provides a falsifiable, data-driven approach: if entanglement indeed induces local geometric shifts, correlated deviations across multiple observables may constitute the first experimentally accessible signatures of ER=EPR physics.

Future work will aim to validate these methods using actual experimental data, incorporate known systematics into the simulations, and investigate the interplay between ER=EPR effects and other vacuum fluctuation phenomena, including dynamical Casimir effects and vacuum birefringence [29, 40]. As summarized in Fig. 4, the experimental landscape provides a clear, falsifiable roadmap by comparing sensitivity and cost across platforms, thereby guiding the prioritization of near-term and next-generation tests of entanglement-induced vacuum modifications.

9. Acknowledgments

The author acknowledges helpful discussions with colleagues in quantum optics, condensed matter, and cosmology, whose feedback improved both the experimental scope and theoretical framing of this work. This research was conducted independently under the Energy Policy and Climate Program at Johns Hopkins University.

This manuscript also benefited from the use of OpenAI's ChatGPT (GPT-4), particularly for LaTeX structuring, technical editing, reference cleanup, and table formatting during manuscript preparation [51, 52]. All scientific content, interpretation, and conclusions are the responsibility of the author.

This work received no external funding. All opinions and conclusions are those of the author and do not represent institutional positions.

Appendix A. Monte Carlo Simulation of Observable Covariances

To validate the PCA component loadings shown in Table App 2, we performed Monte Carlo simulations of $N = 1000$ realizations for the four primary observables: the Casimir force shift ΔF, the Bell correlation parameter S, the squeezing variance ΔV_{sq}, and the optomechanical frequency shift $\Delta\Omega_{\mathrm{om}}$. Each observable was modeled as a Gaussian random variable with mean and variance informed by recent experimental reports [11, 17, 20, 22, 23]. The Gaussian means, variances, and threshold criteria for each observable were chosen according to the simulation parameters summarized in Table App 1, which also specifies the fraction of boosted (correlated) events included in the analysis.

In the *null case*, all three observables were sampled independently, resulting in a single Gaussian cluster in the joint observable space. This corresponds to the experimentally supported expectation that each measurement domain exhibits Gaussian-distributed uncertainties without inter-experimental correlation.

To assess the sensitivity of our PCA method to possible hidden structure, we also introduced a synthetic correlation parameter p_{corr}. With probability p_{corr}, a subset of realizations was coherently shifted across all observables, representing the possibility of systematic deviations that couple different experiments. While no current experimental evidence supports nonzero p_{corr}, a range of $p_{corr} = 0.05{-}0.10$ illustrates how correlated anomalies at this level would produce multiple clusters in the PCA projection, an effect invisible when each observable is considered in isolation.

Principal component analysis was performed by computing the covariance matrix

$$C = \frac{1}{N-1}(X - \bar{X})^T(X - \bar{X}), \tag{A.1}$$

followed by eigen-decomposition

$$Cv_i = \lambda_i v_i, \tag{A.2}$$

with eigenvalues λ_i and eigenvectors v_i defining the component loadings. The loadings reported in Table App 2 correspond to the null case, whereas Fig. App 1 contrasts the single-cluster null simulation with a representative $p_{corr} = 0.08$ case showing two clusters.

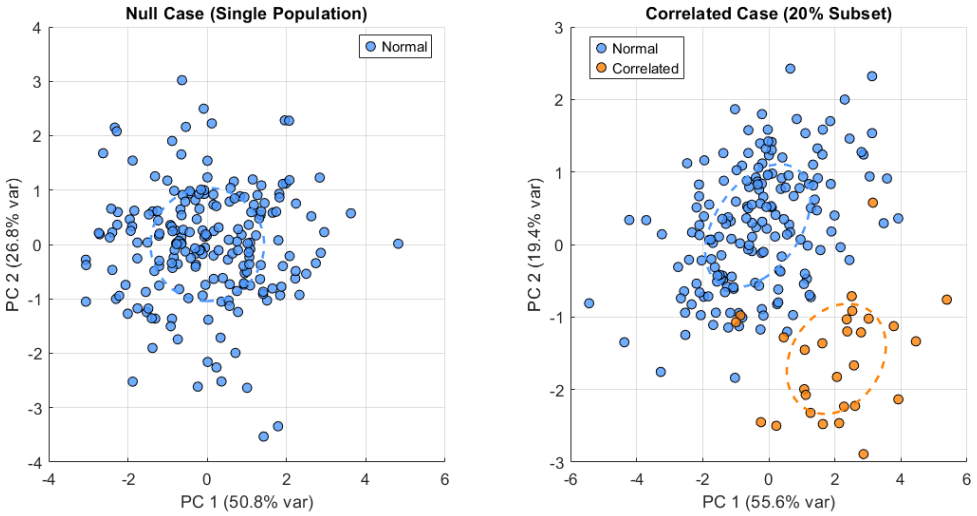

Figure App 1: Principal component analysis (PCA) results comparing the *Null case* (single cluster) with the *Correlated case* (secondary cluster introduced for $p_{\text{corr}} = 0.08$). Light blue points represent the normal population, orange points the correlated subset. Dashed ellipses indicate 1σ confidence regions for each group.

Appendix B. Simulated Projections and Falsification Analysis for ER=EPR Detection

This appendix presents simulated projections of quantum observables under the ER=EPR hypothesis, incorporating experimental sensitivity thresholds. The dataset includes Bell violations (S), Casimir shifts (ΔF), squeezing variance (ΔV_{sq}), and an

optomechanical displacement channel (X_{OM}). A fraction of events were synthetically tagged as correlated to illustrate the emergence of anomalies above the null expectation.

The optomechanical channel was modeled as a Gaussian-distributed variable with an added damped sinusoidal modulation:

$$X_{OM}(t) = \mathcal{N}(0, \sigma^2) + Ae^{-\gamma t}\sin(\omega t + \phi), \tag{B.1}$$

where A, γ, ω, and ϕ are chosen to represent mechanical ringing and delayed response relative to optical observables.

Principal component analysis (PCA) quantifies the contribution of each observable to the first two components:

$$PC_k = w_{k,1}S + w_{k,2}\Delta F + w_{k,3}\Delta V_{sq} + w_{k,4}X_{OM}, \tag{B.2}$$

where $w_{k,i}$ are the normalized weights for component k and observable i. Tables App 1 and App 2 provide input and reports the Monte Carlo PCA loadings, with bold entries exceeding typical sensitivity thresholds.

Appendix B.1. Simulation Parameters for Monte Carlo Analysis

For reproducibility and clarity, Table App 1 summarizes all parameters used to generate the synthetic datasets underlying Tables App 1 and App 3 – Fig. App 4. Each observable (Bell S, Casimir ΔF, HSFL, and optomechanics X_{OM}) was modeled with Gaussian statistics, with a small subset of events boosted to simulate correlated deviations expected under the ER=EPR hypothesis.

Table App 1: Monte Carlo simulation parameters for synthetic observables. These values define the base Gaussian distributions, threshold criteria, and fraction of boosted (correlated) events used in the analysis.

Parameter	Description	Value
N_{ev}	Total number of simulated events	300
N_{boot}	Number of bootstrap resamples for null expectation	10,000
S	Bell observable, standard deviation	1
ΔF	Casimir observable, standard deviation	0.8
HSFL	HSFL observable, standard deviation	0.5
X_{OM}	Optomechanics, Gaussian + damped sinusoid	$1 + 0.3\sin(2\pi t/N_{\text{ev}})$
f_B	Fraction of boosted (correlated) events	0.2
v_{sft}	Boost vector added to correlated events	[1.5, 1.2, 1.4, 1.3]
th_strong	Threshold for strong falsification	2σ
th_weak	Threshold for weak falsification	1σ

These parameters directly determine the per-observable counts exceeding thresholds (O_i) and the PCA component loadings in Tables App 1 and App 2. They also define

the expected counts (E_i) under the null hypothesis for Table App 3. The histogram in Fig. App 4 is generated by counting, for each event, the number of observables simultaneously exceeding the strong threshold, illustrating how boosted correlations shift the distribution relative to the null expectation. Including the optomechanical channel (X_{OM}) ensures that multi-channel coincidences are accurately captured across all four observables.

To quantify the deviation of observed per-event counts from the null hypothesis, we report both a chi-squared statistic and the Kullback–Leibler (KL) divergence. The KL divergence provides an information-theoretic measure of the distance between the empirical distribution and the Gaussian null model, expressed in bits. This complementary measure is sensitive to systematic skew or clustering not captured by variance alone, and is widely used in statistical signal analysis [50]. Table App 3 summarizes the results for the three threshold regions, alongside the corresponding counts for each observable.

Table App 2: Per-observable Monte Carlo counts and statistical measures across threshold regions. O_i are observed counts, E_i expected counts (bootstrap), with chi-squared and KL divergence.

Observable	O_{strong}	O_{weak}	O_{null}	χ^2	D_{KL} [bits]
Bell (S)	25	55	220	0.00015	3.8×10^{-7}
Casimir (ΔF)	17	58	225	0.00006	2.0×10^{-7}
HSFL	8	35	257	0.00042	1.1×10^{-6}
Optomech (X_{OM})	30	55	215	0.00063	1.6×10^{-6}

Time-lagged correlations are computed as

$$Corr_\ell(X,Y) = \frac{1}{N}\sum_t \frac{(X_t - \bar{X})(Y_{t+\ell} - \bar{Y})}{\sigma_X \sigma_Y}. \tag{B.3}$$

Representative pairings include Bell–Casimir, Bell–squeezing, Casimir–squeezing, and squeezing–optomechanics. These four channels capture both direct quantum–vacuum couplings and delayed mechanical responses.

Mutual information between observables highlights nonlinear correlations:

$$I(X,Y) = \sum_{i,j} p_{ij} \log_2 \frac{p_{ij}}{p_i p_j}. \tag{B.4}$$

Finally, multi-channel deviations are summarized by counting events where two or more observables simultaneously exceed the 2σ threshold. Statistical measures include chi-squared and Kullback–Leibler divergence:

$$\chi^2 = \sum_i \frac{(O_i - E_i)^2}{E_i}, \quad D_{KL}(P||Q) = \sum_i P(i) \log_2 \frac{P(i)}{Q(i)}. \tag{B.5}$$

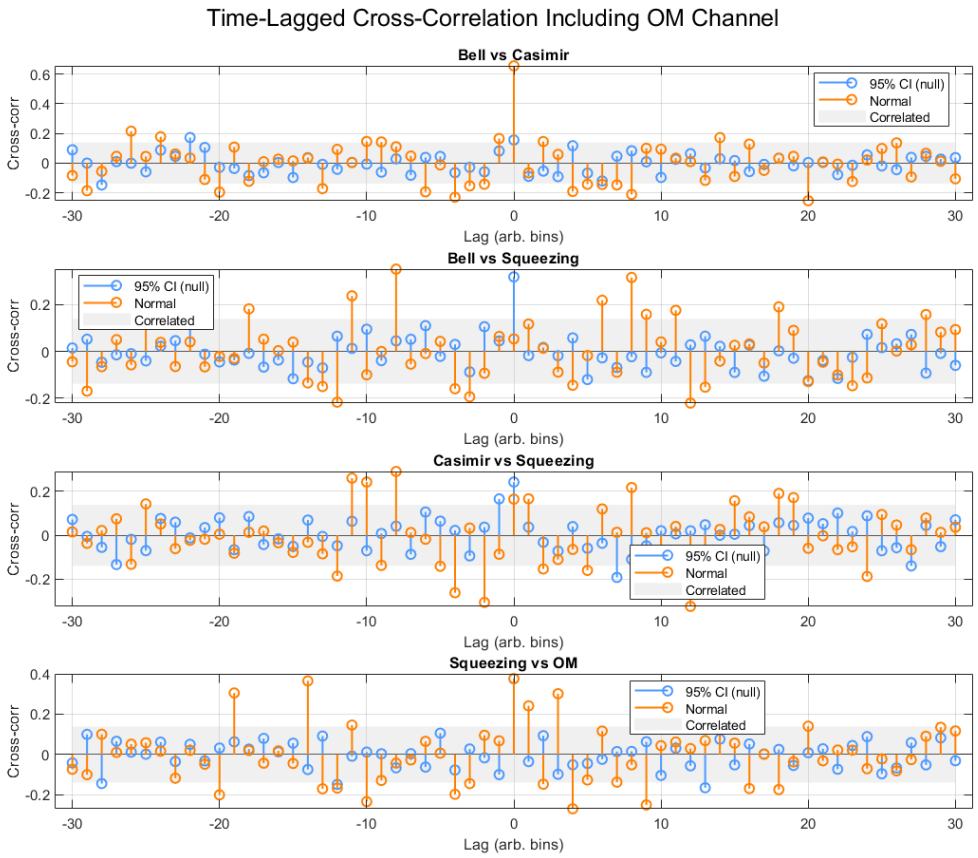

Figure App 2: Time-lagged cross-correlation between four representative observable pairs: (i) Bell–Casimir, (ii) Bell–squeezing, (iii) Casimir–squeezing, and (iv) squeezing–optomechanics to capture delayed mechanical response. Shaded bands show 95% confidence intervals for the Gaussian null; markers above indicate simultaneous events exceeding experimental falsification thresholds. The lag axis is shown in arbitrary units corresponding to sampling bins; for high-speed acquisition, one bin may correspond to ∼ns, while for lower-bandwidth detectors it could represent μs or longer.

Appendix C. Statistical Complement to Falsification Diagrams

This appendix provides a statistical framework complementing the falsification diagrams presented in Sec. V. Each event is analyzed across the observables relative to the sensitivity-based thresholds derived from the SNR scaling (Fig. 2). Observables exceeding the strong falsification line are assigned to the *strong falsification region* (yellow); those between the weak and strong thresholds are assigned to the *weak falsification region* (gray); remaining events fall in the *null region* (unshaded). This classification enables a per-event assessment of significance across Bell (S), Casimir (ΔF), HSFL, and optomechanics (X_{OM}).

Figure App 5 illustrates the workflow connecting the synthetic Monte Carlo simulations to the statistical analyses and figures in the appendices. The simulations

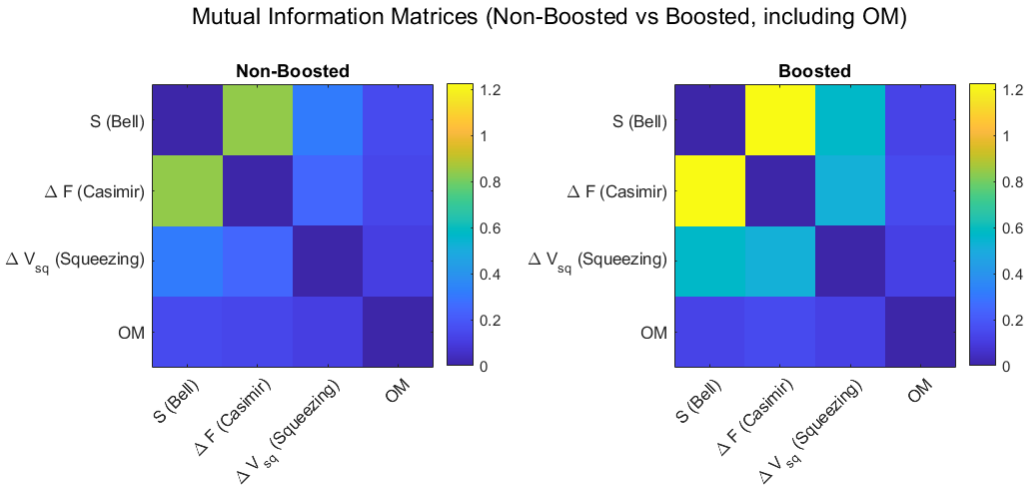

Figure App 3: Mutual information matrices for Bell (S), Casimir (ΔF), squeezing (ΔV_{sq}), and optomechanics (X_{OM}), shown for non-boosted (left) and boosted (right) datasets. Off-diagonal entries above the falsification threshold are outlined. The comparison highlights how boosting modifies nonlinear dependencies across optical, mechanical, and hybrid observables.

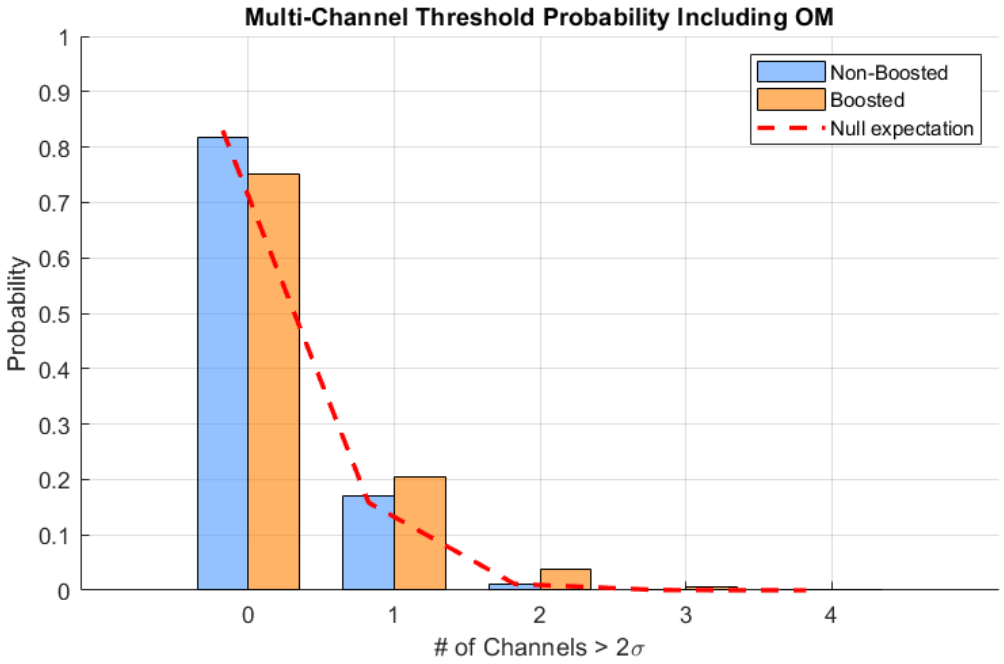

Figure App 4: Probability of each event exceeding a 2σ threshold in 0–4 observables ("channels") per simulated event. The four channels are Bell (S), Casimir (ΔF), squeezing (ΔV_{sq}), and optomechanics (X_{OM}). Blue bars show the non-boosted subset, orange bars show the boosted (correlated) subset, and the red dashed line indicates the null expectation from a large Gaussian ensemble. Boosted correlations increase the probability of multi-channel coincidences (2–4 channels), while non-boosted events remain concentrated at 0–1 channels.

generate the four observables (Bell S, Casimir ΔF, HSFL, and optomechanics X_{OM}). Principal component analysis (Table App 1) identifies the dominant contributions to variance, while per-event threshold counts (Table App 2) quantify the number of events exceeding weak and strong falsification thresholds. Multi-channel histograms (Fig. A4) summarize the distribution of events across multiple observables, and cross-correlation or mutual information plots (Figs. A2–A3) capture interactions among observables. This diagram provides a clear roadmap linking simulations, statistical tables, and visual analyses.

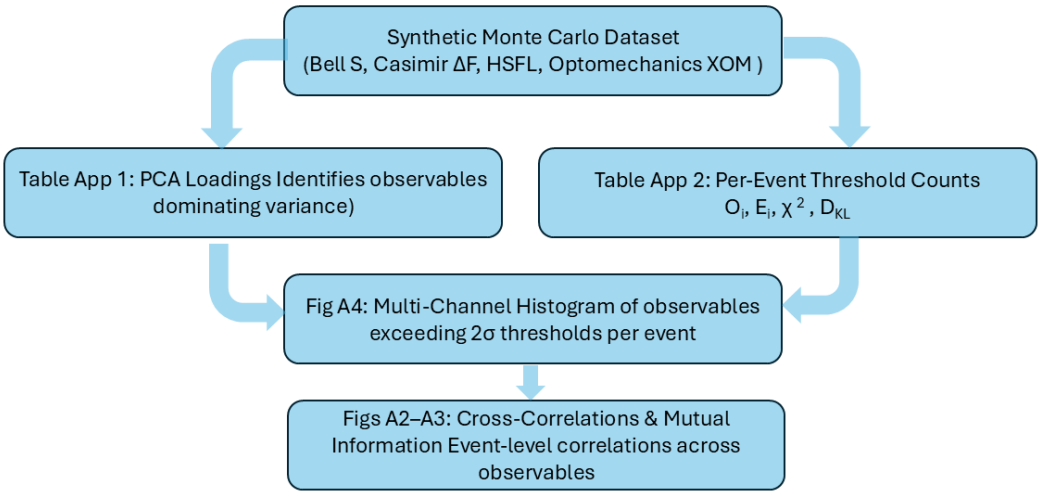

Figure App 5: Flow diagram connecting the synthetic Monte Carlo dataset to Appendix Table App 1-Table App 2 and Figures App 1 PCA highlight key observables, per-event threshold counts (Table App 3) quantify individual significance, multi-channel histograms (Fig.App 4) summarize event-level coincidences, and cross-correlation/mutual information plots (Figs. App 2-App 3) capture interactions among observables.

Observed counts O_i in each region are generated via synthetic Monte Carlo simulations of $N_{\text{ev}} = 300$, while expected counts E_i are computed using $N_{\text{boot}} = 10^4$ bootstrap resamplings under the null hypothesis. Deviations between observed and expected counts are quantified with chi-squared and Kullback–Leibler divergence:

$$\chi^2 = \sum_i \frac{(O_i - E_i)^2}{E_i}, \quad D_{\text{KL}}(P||Q) = \sum_i P(i) \log_2 \frac{P(i)}{Q(i)}, \tag{C.1}$$

where $P(i) = O_i/N_{\text{ev}}$ and $Q(i) = E_i/N_{\text{ev}}$ are the observed and null probabilities for each threshold region. Elevated χ^2 or D_{KL} values indicate deviations potentially exceeding statistical expectations under the null hypothesis.

Statistical power for detection is estimated as The statistical power, Power $= 1-\beta$, represents the probability of detecting a deviation Δ in the strong or weak falsification region, given that a true signal exists.

Table App 3: Per-event Monte Carlo counts and statistical measures across threshold regions. Observed counts O_i, expected counts E_i, chi-squared, and KL divergence are shown for four observables: Bell (S), Casimir (ΔF), HSFL, and optomechanics (X_{OM}). Threshold categories correspond to the shaded regions in Fig. 2: strong falsification (yellow), weak falsification (gray), and null region (unshaded).

Threshold Region	S	ΔF	HSFL	X_{OM}	χ^2	D_{KL} [bits]
Strong falsification (yellow)	25	17	8	30	0.0013	3.9e-06
Weak falsification (gray)	55	58	35	55	0.0012	3.7e-06
Null region (unshaded)	220	225	257	215	0	0

This unified presentation directly links the SNR-based threshold diagrams (Fig. 2) to quantitative statistical metrics, providing a clear interpretation of potential ER=EPR-induced anomalies across Bell, Casimir, HSFL, and optomechanical observables.

Appendix D. Normalization of Observables for Falsification Diagrams

This appendix details how raw perturbations in each module (Bell, Casimir, squeezing, spectroscopy loop) are converted into normalized deviations Δ that define the axes of the falsification diagrams (Figs. 2–3). These mappings link the equations of Sec. 2 to the sensitivity thresholds used in the falsification framework.

Appendix D.1. Bell Observable

From Eq. (2), the measured Bell parameter is

$$S(d) = S_0 + \delta S(d), \tag{D.1}$$

where S_0 is the baseline and $\delta S(d)$ is the perturbation arising from vacuum-induced modifications. For the falsification diagrams, we plot the normalized deviation

$$\Delta_S = \frac{\delta S}{S_0}. \tag{D.2}$$

This defines the Bell-threshold curve shown in the sensitivity plots.

Appendix D.2. Casimir–Optomechanical Displacement

The entanglement-modified observable is written in Eq. (3) as

$$\Delta X = X_{\mathrm{ent}} - X_0, \tag{D.3}$$

with X_0 the baseline value. The corresponding falsification variable is the fractional shift

$$\Delta_X = \frac{\Delta X}{X_0}. \tag{D.4}$$

The SQL bound [Eq. (14)] sets the lower detection boundary for Δ_X as plotted in Figs. 2–3.

Appendix D.3. Optical Squeezing Parameter

The squeezed variance is given by Eq. (5):

$$\Delta^2 X_{\text{squeezed}} = \frac{\hbar}{2} e^{-2r}. \tag{D.5}$$

A geometry-induced perturbation in the squeezing parameter r produces

$$\delta r(d) \sim \alpha \frac{\partial r}{\partial d}. \tag{D.6}$$

In the falsification diagrams, this is tracked as the normalized change

$$\Delta_r = \frac{\delta r}{r}, \tag{D.7}$$

which contributes to shifts in the Bell observable curve.

Appendix D.4. Spectroscopy Loop Phase Shift

The loop phase shift is defined in Eq. (7) as

$$\delta\phi_{\text{loop}} = \frac{4\pi L}{\lambda} \frac{\delta n}{n}. \tag{D.8}$$

Normalizing by the reference phase $\phi_{\text{ref}} = 4\pi L/\lambda$, the falsification variable becomes

$$\Delta_\phi = \frac{\delta\phi_{\text{loop}}}{\phi_{\text{ref}}} = \frac{\delta n}{n}. \tag{D.9}$$

In summary, all raw perturbations are cast into dimensionless fractions:

$$\Delta_S, \quad \Delta_X, \quad \Delta_r, \quad \Delta_\phi,$$

which form the axes and thresholds of the falsification diagrams (Figs. 2–3). This normalization ensures direct comparability across Bell, Casimir, squeezing, and optomechanical observables, and links the qualitative mechanisms in Table 1 to the quantitative sensitivity analysis.

References

[1] J. Maldacena, "Non-Gaussian features of primordial fluctuations in single field inflationary models," *J. High Energy Phys.*, vol. 2003, no. 5, p. 013, 2003. doi:10.1088/1126-6708/2003/05/013.

[2] J. Maldacena and L. Susskind, "Cool horizons for entangled black holes," *Fortschr. Phys.* **61**, 781 (2013), doi:10.1002/prop.201300020.

[3] A. Pisani, E. Massara, and M. Viel, "Cosmic voids: a novel probe to shed light on our Universe," *Physics Reports*, vol. 804, pp. 1–56, 2019. doi:10.1016/j.physrep.2019.07.002.

[4] L. Susskind, "ER=EPR, GHZ, and the consistency of quantum measurements," *Fortschr. Phys.* **64**, 72 (2016), doi:10.1002/prop.201500094.

[5] M. Van Raamsdonk, "Building up spacetime with quantum entanglement," *Gen. Rel. Grav.* **42**, 2323–2329 (2010), arXiv:1005.3035 [hep-th].

[6] R. Garattini, "Effects of Planck-scale wormholes on the cosmological constant problem," *Eur. Phys. J. C* **79**, 951 (2019).

[7] E. P. Verlinde, "On the origin of gravity and the laws of Newton," *Journal of High Energy Physics*, vol. 2011, no. 4, p. 29, 2011. doi:10.1007/JHEP04(2011)029.

[8] A. Aspect, J. Dalibard, and G. Roger, "Experimental Test of Bell's Inequalities Using Time–Varying Analyzers," *Phys. Rev. Lett.* **49**, 1804 (1982).

[9] D. Rauch et al., "Cosmic Bell Test Using Random Measurement Settings from High-Redshift Quasars," *Phys. Rev. Lett.* **121**, 080403 (2018).

[10] P. G. Kwiat et al., "New High-Intensity Source of Polarization-Entangled Photon Pairs," *Phys. Rev. Lett.* **75**, 4337 (1995).

[11] B. Hensen, H. Bernien, A. Dréau, et al., "Loophole-free Bell inequality violation using electron spins separated by 1.3 kilometres," *Nature* **526**, 682–686 (2015).

[12] W. H. Zurek, "Decoherence, einselection, and the quantum origins of the classical," *Rev. Mod. Phys.* **75**, 715 (2003), doi:10.1103/RevModPhys.75.715.

[13] H. B. G. Casimir, "On the attraction between two perfectly conducting plates," *Proc. K. Ned. Akad. Wet.* **51**, 793 (1948).

[14] S. K. Lamoreaux, "Demonstration of the Casimir force in the 0.6 to 6 μm range," *Phys. Rev. Lett.* **78**, 5 (1997).

[15] S. K. Lamoreaux, "The Casimir force: Still surprising after 60 years," *Phys. Today* **58**(2), 40 (2005).

[16] E. Buks and M. L. Roukes, "Stiction, adhesion energy, and the Casimir effect in micromechanical systems," *Phys. Rev. B* **63**, 033402 (2001).

[17] D. F. Walls, "Squeezed states of light," *Nature* **306**, 141 (1983).

[18] E. D. Black, "An introduction to Pound–Drever–Hall laser frequency stabilization," *Am. J. Phys.* **69**, 79 (2001).

[19] R. W. P. Drever et al., "Laser phase and frequency stabilization using an optical resonator," *Appl. Phys. B* **31**, 97 (1983).

[20] R. E. Slusher et al., "Observation of squeezed states generated by four-wave mixing in an optical cavity," *Phys. Rev. Lett.* **55**, 2409–2412 (1985).

[21] M. P. Blencowe, "Quantum Optomechanics: Nanomechanics with Radiation Pressure," *Physics Reports*, vol. 395, no. 6, pp. 159–172, 2013. doi:10.1016/j.physrep.2004.10.001

[22] J. Chan et al., "Laser cooling of a nanomechanical oscillator into its quantum ground state," *Nature* **478**, 89 (2011).

[23] Markus Aspelmeyer, Tobias J. Kippenberg, and Florian Marquardt, "Cavity Optomechanics," *Reviews of Modern Physics*, Vol. 86, No. 4, 1391–1452 (2014). doi:10.1103/RevModPhys.86.1391

[24] E. Verhagen et al., "Quantum-coherent coupling of a mechanical oscillator to an optical cavity mode," *Nature* **482**, 63 (2012).

[25] Y. Chen, "Macroscopic quantum mechanics: Theory and experimental concepts of optomechanics," *J. Phys. B: At. Mol. Opt. Phys.* **46**, 104001 (2013).

[26] C. M. Caves, "Quantum-mechanical noise in an interferometer," *Phys. Rev. D* **23**, 1693 (1981).

[27] K. Pearson, "On lines and planes of closest fit to systems of points in space," *Philosophical Magazine* **2**, 559 (1901).

[28] T. M. Cover and J. A. Thomas, *Elements of Information Theory*, (Wiley, New York, 1991).

[29] C. Sabín et al., "Phonon creation by gravitational waves," *New J. Phys.* **16**, 085003 (2014).

[30] D. E. Bruschi et al., "Relativistic motion generates entanglement," *Phys. Rev. D* **87**, 125018 (2013).

[31] E. Martín-Martínez et al., "Entangled quantum fields and the Einstein-Rosen bridge," *Phys. Rev. D* **104**, 045015 (2021).

[32] M. Kjaergaard, M. E. Schwartz, and J. R. Petta, "Quantum dots as stationary sources of entangled electron pairs," *Nature Reviews Physics*, vol. 2, no. 12, pp. 617–630, 2020. doi:10.1038/s41567-020-0805-0.

[33] NANOGrav Collaboration, "The NANOGrav 15-year Data Set: Evidence for a Gravitational-Wave Background," *The Astrophysical Journal Letters*, vol. 951, no. 1, p. L9, 2023. doi:10.3847/2041-

8213/ac6f24.

[34] IPTA Collaboration, "The International Pulsar Timing Array: Second Data Release," *Mon. Not. R. Astron. Soc.* **482**, 3100–3124 (2019). doi:10.1093/mnras/sty2910.

[35] CMB-S4 Collaboration, "CMB-S4 Science Case, Reference Design, and Project Plan," *Fermilab-Pub-19-431-AE-SCD*, 2019. Available: `https://lss.fnal.gov/archive/2019/pub/fermilab-pub-19-431-ae-scd.pdf`.

[36] LiteBIRD Collaboration, "The LiteBIRD Mission to Explore Cosmic Inflation," *PTEP*, vol. 2023, no. 4, p. 042F01, 2023. Available: `https://academic.oup.com/ptep/article/2023/4/042F01/6835420`.

[37] Euclid Collaboration, "Euclid: Mapping the geometry of the dark Universe," *Astron. Astrophys.*, 2020, arXiv:1910.09273.

[38] Roman Collaboration, "Nancy Grace Roman Space Telescope: Science Overview," *Proc. SPIE*, vol. 11443, 2021.

[39] LSST Science Collaboration, "LSST Science Book, Version 2.0," arXiv:0912.0201 [astro-ph.IM], 2009.

[40] C. J. Hogan, "Interferometers as probes of Planckian quantum geometry," *Phys. Rev. D* **85**, 064007 (2012). doi:10.1103/PhysRevD.85.064007.

[41] O. Kwon, H. R. Gustafson, B. L. Kamai, J. W. Richardson, and C. J. Hogan, "Interferometric constraints on quantum geometrical shear noise correlations," *Classical and Quantum Gravity*, vol. 34, no. 23, p. 234001, 2017. doi:10.1088/1361-6382/aa8f3b.

[42] G. E. Stedman, "Ring-laser tests of fundamental physics and geophysics," *Reports on Progress in Physics*, vol. 60, no. 6, pp. 615–688, 1997. doi:10.1088/0034-4885/60/6/002

[43] W. F. McGrew et al., "Atomic clock performance enabling geodesy below the centimetre level," *Nature* **564**, 87 (2018).

[44] M. Abe et al., "Matter-wave Atomic Gravitational Wave Interferometric Sensor (MAGIS-100)," *Quantum Sci. Technol.* **6**, 044003 (2021).

[45] K. Bongs et al., "Taking atom interferometric quantum sensors from the laboratory to real-world applications," *Nat. Rev. Phys.* **1**, 731 (2019).

[46] L. Badurina et al., "AION: An Atom Interferometer Observatory and Network," *JCAP* **05**, 011 (2020).

[47] LIGO Scientific Collaboration and Virgo Collaboration, "Constraints on cosmic strings using data from the first Advanced LIGO observing run," *Phys. Rev. D* **104**, 022004 (2021). doi:10.1103/PhysRevD.104.022004.

[48] P. Amaro-Seoane et al., "Laser Interferometer Space Antenna," *arXiv:1702.00786 [astro-ph.IM]*, 2017.

[49] M. Punturo et al., "The Einstein Telescope: A third-generation gravitational wave observatory," *Classical and Quantum Gravity*, vol. 27, 194002, 2010.

[50] S. Kullback and R. A. Leibler, "On Information and Sufficiency," *Annals of Mathematical Statistics* **22**, 79–86 (1951).

[51] OpenAI, "ChatGPT (GPT-5) Technical Capabilities and Usage," OpenAI, 2025. Available at: `https://openai.com/research`.

[52] OpenAI, "GPT-4 Technical Report," 2023. Available at: `https://openai.com/research/gpt-4`.